Assessment of Traveling Wave-Based Functions in Inverter-Based Resource Interconnecting Lines

Felipe V. Lopes, Moisés J. B. B. Davi, Mário Oleskovicz

***Abstract*—In this paper, the behavior of traveling waves (TWs) on transmission lines which interconnect inverter-based resources (IBRs) is investigated, assessing the performance of well-known TW functions applied in protection and fault location schemes. To do so, traditional synchronous generators and wind turbine-based IBRs of types III and IV are investigated, allowing comparative studies regarding the shape of fault-induced transients measured at the monitored line terminals. Then, the impacts of typical terminations of IBR-interconnecting lines on the classical double-ended TW-based fault location method, as well as on directional, overcurrent and differential TW-based protections are analyzed, highlighting the effects of busbar and transformer stray capacitances on the performance of these functions. The obtained results reveal that TW solutions are promising for IBR-interconnecting lines. However, a significant influence of busbar and transformer stray capacitances on the performance of TW functions is also identified, revealing the need for taking these capacitances into account during the definition of settings used in TW protection and fault location schemes.**

***Keywords*—Electromagnetic transients, fault location, IBR, power system, protection, traveling wave.**

I. Introduction

THE increasing use of renewable generation in electrical power grids has boosted several studies about the performance of protection and fault location schemes on IBR-interconnecting lines [1]–[3]. Among the existing IBRs, photovoltaic power plants and wind turbine-based IBRs (WIBRs) of types III (Doubly-Fed Induction Generator – DFIG) and IV (Full Converter – FC) have been widely studied.

Since IBRs are dictated by their associated inverter controls [4]–[6], they behave differently from traditional synchronous generators, resulting in atypical short-circuit contributions that can affect classical fundamental component-based protection and fault location methods [1]–[3]. Hence, researches have been conducted toward identifying innovative protection and fault location solutions, among which TW-based functions are often reported as promising. Indeed, since they depend basically on the evaluation of amplitudes, polarities and travel times of high frequency TWs, issues caused by IBR-induced atypical behaviors of voltages and currents at the fundamental frequency are overcome [3], [7]. However, IBR-interconnecting circuits typically consist of transformer-terminated lines, resulting in strong inductive behavior at IBR side, which can affect TW functions [7], [8].

F. V. Lopes is with Federal University of Paraíba (UFPB), Brazil (email: felipelopes@cear.ufpb.br).

Moisés J. B. B. Davi and Mário Oleskovicz are with University of São Paulo (USP), Brazil (email: moisesdavi@usp.br, olesk@sc.usp.br).

Paper submitted to the International Conference on Power Systems Transients (IPST2023) in Thessaloniki, Greece, June 12-15, 2023.

In transformer-terminated lines, the substation stray capacitances become an important aspect to understand the distortions and shapes of measured TWs. Some effects of busbar and transformer stray capacitances have been studied in [7], [8]. However, from the authors' best knowledge, comprehensive sensitivity assessments regarding the influence of stray capacitances on different TW-based protection and fault location functions is still a topic that needs further clarifications. Thus, in this paper, a thorough study is carried out to analyze the performance of TW-based directional, overcurrent, and differential protections, as well as of the classical double-ended TW-based fault location method when applied to an IBR-interconnecting line. WIBR models of types III (DFIG) and IV (FC) and the associated interconnecting circuit are modeled and simulated in PSCAD, allowing to evaluate similarities between the shapes of filtered TWs for different generation types with different control schemes, and to assess the operating conditions of each analyzed TW function. The obtained results confirm that TW-based solutions are promising for IBR-interconnecting lines. However, the influence of line terminations is demonstrated, revealing that busbar and transformer stray capacitances can be decisive to the performance of TW-based applications.

II. Typical IBR-Interconnecting Circuit

In Fig. 1, a typical IBR-interconnecting circuit is presented. Here, WIBRs of types III (DFIG) and IV (FC) with different control schemes are assumed to be connected at Bus L (local bus), one type per evaluated scenario, whereas Bus R (remote bus) is taken as the connection point to the grid, representing a typical strong terminal. Such a network is taken as the test system, being all simulations run in PSCAD. WIBRs are modeled according to [9], [10] with few adaptations to emulate operation requirements reported in [11], whereas the rest of the system is modeled as in [3], [7], considering different fault points (F1, F2 and F3) as shown in Fig. 1.

In the test system, IBRs are connected to a distribution feeder, which converges to a step-up YNd1 transformer that elevates voltages to sub-transmission levels. The system follows with sub-transmission lines until another YNyn0 step-up transformer, which increases voltages to the desired transmission levels. The grid connection is provided by means of a 500 kV/60 Hz transmission line, which is the focus of this work. Although one knows that IBR controls can affect classical fundamental component-based line monitoring functions, this paper focuses on the study of TWs, highlighting the impacts of IBR-terminal busbar and transformer stray capacitances on TW-based applications.

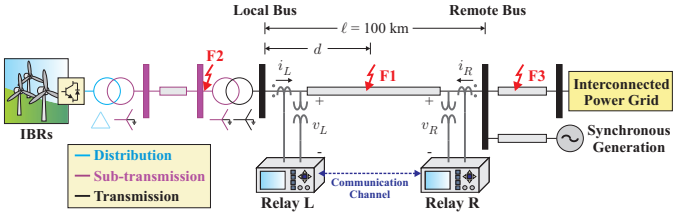

Fig. 1. Typical topology of IBR-interconnecting circuits.

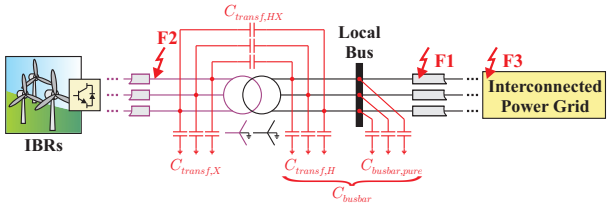

Fig. 2. Stray capacitances at the IBR connection terminal.

In the test system (see Fig. 1), since the local line terminal is terminated by a transformer, the Bus L termination presents a strong inductive characteristic. In practice, the termination effects are superposed by those from stray capacitances on the busbar ($C_{busbar,pure}$) and on the transformer, between low and high voltage windings ($C_{transf,HX}$), between the low voltage winding and the ground ($C_{transf,X}$), as well as between the high voltage winding and the ground ($C_{transf,H}$), as shown in Fig. 2. Here, since $C_{transf,H}$ and $C_{busbar,pure}$ are in parallel, only the equivalent busbar stray capacitance $C_{busbar} = C_{transf,H} + C_{busbar,pure}$ is modeled.

III. Theoretical Background on Measured TWs

As a first investigation step on the shape of TWs on transformer-terminated lines, Fig. 3 shows records for an AG solid fault applied at point F1 on the test system shown in Fig. 1. Only the faulted phase is presented in the figure. C_{busbar} values are adjusted as reported in [7]. Three different scenarios are simulated, considering three generation types, one per graphic, namely: conventional synchronous generator, DFIG-WIBR and FC-WIBR. Also, the fault inception angle θ is varied, adopting $\theta = 0°$, $\theta = 45°$ and $\theta = 90°$ to provide a first analysis on whether the behavior of fault-induced transients change for different generation types.

Fig. 3 shows that different fault contribution levels occur for the analyzed generations. Also, it reveals that the DC decaying component is reduced for both DFIG and FC WIBRs in comparison to the synchronous generator. However, the interest here is to analyze fault-induced transients related to the TW phenomena and, as shown in the zoomed areas, there are evidences that high frequency transients follow the traditional behavior. Indeed, the signal transient content increases if $\theta \approx 90°$ (or $270°$, i.e., fault inception at the voltage peak) and decreases if $\theta \approx 0°$ (or $180°$, i.e., fault inception at voltage zero crossing). Such a behavior is noticed for the three evaluated generation types, consisting in an initial evidence that TWs may not be relevantly affected by IBR controls. Indeed, it is known that amplitudes and polarities of fault-launched TWs depend on the line characteristic impedance, fault resistance and voltages at the fault point at the disturbance inception instant (which depends on θ) [12]. Hence, if different IBR controls somehow result in different pre-fault voltage profiles over the line, the amplitudes of TWs are expected to change. However, if two different IBR control schemes result in the same line pre-fault voltage profile, fault-launched TWs will be the same for both systems, such that the format of measured TWs will depend basically on the line termination characteristics [13], [14].

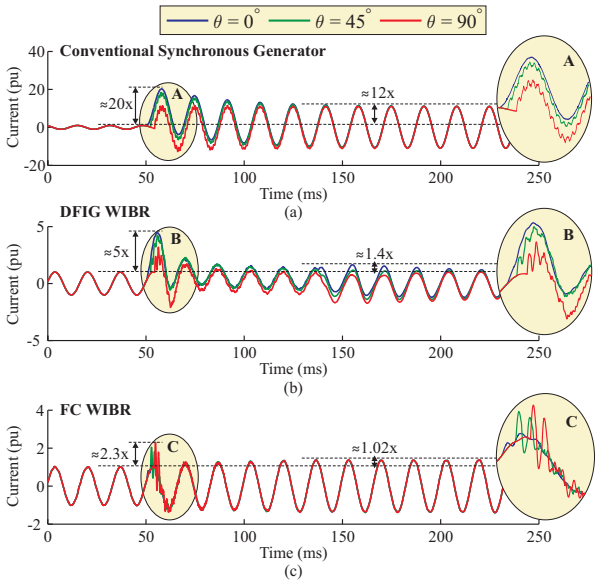

Fig. 3. Comparative analysis between fault contributions obtained for different fault inception angles θ coming from: (a) Conventional synchronous generator; (b) DFIG-WIBR; (c) FC-WIBR.

To evaluate measured wavefronts, the reflection coefficients for current TWs (TWI) and voltage TWs (TWV) at both line ends must be analyzed, which are given by [14]:

$$\Gamma_I = \frac{Z_c - Z_T}{Z_T + Z_c}\ , \tag{1}$$

$$\Gamma_V = \frac{Z_T - Z_c}{Z_T + Z_c}\ , \tag{2}$$

where Γ_I and Γ_V are the reflection coefficients for TWI and TWV, respectively, being Z_c the line characteristic impedance and Z_T the terminal impedance at the measurement point. At higher frequencies, $Z_c \approx Z_s$, being Z_s the line surge impedance [14]. Thus, since TWs are analyzed in this paper, (1) and (2) are calculated for $Z_c = Z_s$.

Due to the strong inductive characteristic of power transformers, at Bus L, TWs see an open circuit [7], [8]. Thus, $Z_T \to \infty$, such that $\Gamma_I \approx -1$ and $\Gamma_V \approx +1$. It means that TWIs are reflected with opposite polarity in relation the incident wavefronts, whereas reflected TWVs present the same polarity. It leads TWIs to be attenuated and TWVs to be amplified. Even so, voltage measurements in transmission lines are typically obtained from capacitive voltage transformers, which have poor frequency response [15]. Therefore, most TW functions analyze TWIs, with the exception of some approaches which evaluate only the arrival times of the first incident TWVs at the line terminals.

It is worth noting that stray capacitances may change the behavior of TWs, reducing the attenuation and amplification levels of TWIs and TWVs, respectively. Therefore, when a fault occurs on the power transformer low voltage side (point F2 in Fig. 1), TWIs measured on the high voltage line side present reduced amplitudes due to two main reasons: 1) voltage level at the fault point is lower than the one on the line side; 2) fault-launched TWIs travel to the line side passing through the transformer and busbar stray capacitances, which usually present low values, further attenuating the TWs [8].

From the perspective of TW-based protection functions, it is known that existing approaches require the detection of fault-induced wavefronts, which is typically carried out by comparing measured TWs with detection thresholds. As the amplitude of measured TWs depend on the line terminations, as explained earlier, the wave detection thresholds must be adjusted to guarantee sensitivity, but without compromising the protection security. In this sense, very low threshold settings can compromise the protection security, leading it to operate for low energy transients related to non-fault events. On the other hand, by increasing these thresholds, the protection sensitivity decreases, so that only TWs with very high energy can be detected. Therefore, when transformer-terminated lines are considered, the attenuation/dispersion caused by the transformer inductive behavior can jeopardize the performance of TW-based protection functions, as it will be addressed in the next sections. Indeed, although the analyzed functions have different operation principles, all of them depend on TW detection procedures, evidencing the relevance of the proposed study on the performance of TW functions on IBR-interconnecting lines.

It is also important to understand that, when TWs arrive at the transformer termination (see Fig. 1), considering the presence of the stray capacitances, an equivalent terminal impedance is seen by the waves. For the sake of simplification, one can understand such an equivalent impedance as a parallel association between stray capacitances that branch off Bus L and the transformer inductance. Hence, since TWs see capacitances as low impedance propagation paths [14], at Bus L, as the stray capacitances increase, Z_T tends to zero in (1) and (2), such that Γ_I increases and Γ_V decreases, favoring current and voltage measurements, respectively. Thereby, studying the impacts of stray capacitances in transformer-terminated lines, such as those which connect IBRs, is of utmost importance to properly understand the performance of TW-based functions in this type of system.

IV. Investigation on the Features of TWs in IBR-Interconnecting Lines

Based on the initial evidences that TWs may not be relevantly affected by IBR control strategies, a thorough investigation about the shape of TWs and impacts of stray capacitances is presented in this section. To do so, massive fault simulations on a typical IBR interconnecting system are carried out, evaluating the behavior of TWs by means of TW filters that remove the fundamental component from the obtained measurements.

A. Test System and Testing Methodology

From this section on, results obtained from PSCAD fault simulations will be studied. The test power system shown in Fig. 1 is considered, assuming that the monitored transmission line length is $\ell = 100$ km, being the adjacent line 147 km long. In internal fault cases (point F1), faults at distances $d = 30$ km and 70 km from Bus L are studied. On the other hand, in external fault scenarios, short-circuits on the transformer low voltage terminal (point F2) and on the adjacent transmission line, 7.35 km far from Bus R (point F3), are simulated. For AG faults, fault resistances $R_f \approx 0\ \Omega$ (solid fault) and 100 Ω are taken into account, whereas $R_f \approx 0\ \Omega$ (solid fault) and 1 Ω are evaluated for AB faults. In addition, the stray capacitances are varied, such as: $C_{transf,HX} = [0\ 1\ 2\ 3]$ nF, $C_{transf,X} = [0\ 3\ 7\ 10]$ nF, and $C_{busbar} = [0\ 5\ 15\ 50]$ nF. Hence, a total amount of 1024 fault scenarios are studied, consisting of 64 stray capacitance combinations for each considered fault scenario.

Analyzed fault cases are generated by varying simulations within loops that consider the following order (from innermost to outermost variables): $R_f \rightarrow C_{transf,HX} \rightarrow C_{transf,X} \rightarrow C_{busbar}$. Such information is useful to understand the 'Studied Scenario Number' in the graphics of results. Even so, to facilitate the analysis, the 'increasing stray capacitance direction' is indicated by arrows in all figures, i.e., the first and last scenarios are those in which the lowest and highest stray capacitance values were considered, respectively.

Fig. 4 shows the test system modeled in PSCAD. A time-step equal to 1 μs and a maximum simulation time equal to 0.1 s were used. The synchronous network was modeled by means of Thevenin equivalents, whereas the IBR models were implemented following guidelines reported in [9]–[11]. The equivalent IBR unit shown in Fig. 4 represents a power plant composed by 147 WIBRs of 1.5 MW each, totaling a generation capacity of 220.5 MW. The WIBR models include 0.69/34.5 kV step-up transformers, so that they are not shown in Fig. 4. However, the 34.5/138 kV and 138/500 kV step-up transformers applied to elevate terminal WIBR voltages until transmission levels are explicitly modeled, as shown in Fig. 4. A frequency-dependent transposed line model is used, being the line divided into various sections to allow simulations of faults at different locations. At both line ends, C_{busbar} is modeled, whereas $C_{transf,X}$ and $C_{transf,HX}$ are considered only at the WIBR side (see Figs. 2 and 4). Finally, it is worth mentioning that a script code was used to automatically simulate the studied cases, providing a more comprehensive sensitivity analysis. By doing so, COMTRADE files could be generated for each simulation, allowing to externally apply the analyzed protection functions, which were implemented following instructions reported in [15]–[17].

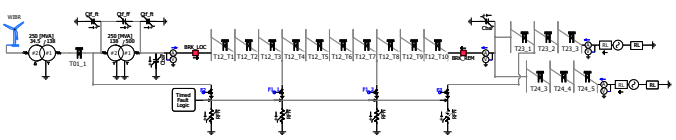

Fig. 4. Test power system modeled in PSCAD.

B. TW Similarity Study for Systems with DFIG and FC

To evaluate whether TWs are affected by different IBR types, AG and AB faults with $\theta = 90^\circ$ at points F1, F2 and F3 are simulated, assuming DFIG and FC WIBRs with different control schemes connected at Bus L (see Fig. 1). In each case, filtered TW information is obtained through the Differentiator-Smoother filter (DS filter) proposed in [18]. Such a filter generates triangular-shaped outputs with unitary gain in response to step changes in input signals induced by arriving TWs. If fault transients are attenuated, ramp changes in input signals are observed rather than step variations, so that the DS filter responds with parabola-shaped outputs. In both cases, the peak values of the triangular/parabola-shaped outputs consist in good amplitude/polarity estimations of TWs, which are widely used in TW applications. By using this filter, one can analyze TWs independently of the fundamental component, which is known to be affected by the IBR controls. Here, the DS filter is implemented according to the validated computational model reported in [19].

The similarity of filtered TWs (DS filter outputs) when DFIG and FC WIBRs are connected at Bus L is evaluated in Fig. 5, where R^2 coefficients[1] [20] are calculated from filtered modal TWs measured at Bus L. In each case, a data window of 1 ms after the fault inception instant is analyzed, using Clarke's transformation to obtain modal TWs [15], which are referred to here via indexes 0 (ground), 1 (aerial α) and 2 (aerial β. To avoid distortions due to measurement devices, ideal instrument transformers are used, adopting voltage and current transformation ratios equal to 4350 and 80, respectively.

Fig. 5(a) demonstrates that TW0s (ground mode TWs) are not relevantly affected by variations in stray capacitances when the fault takes place on the transmission line side. On the other hand, for faults on the power transformer low voltage side, R^2 coefficients decrease. Even so, such coefficients remain greater than 0.75, indicating a satisfactory agreement between the analyzed signals. Regarding the aerial mode TWs (TW1s and TW2s), as depicted in Figs. 5(b) and (c), R^2 coefficients also approximate to 1.0 in most analyzed cases, presenting a reduction for TWIs when low C_{busbar} and $C_{transf,HX}$ values are taken into account. In these scenarios, when C_{busbar} and $C_{transf,HX}$ are low, the amplitude of current TWs is reduced, leading transients imposed by the IBRs to be more prominent, which results in more discrepancies between TWIs for systems with DFIG and FC WIBRs. However, as C_{busbar} and $C_{transf,HX}$ get higher, R^2 coefficients increase, revealing that TW1s and TW2s for DFIG and FC generations are expected to be very similar between each other for practical C_{busbar} and $C_{transf,HX}$ values, even considering different control schemes. Therefore, once the similarity is proven, only FC WIBRs are considered in the next sections.

C. Influence of Stray Capacitances on Measured TWs

Fig. 6 depicts the obtained filtered TWs at buses L and R for faults at points F1 and F2, considering different busbar and transformer stray capacitances. Only TWIs are analyzed, since they are those processed by most existing TW functions.

[1] R^2 coefficients consist in a statistical measure that shows how well two sets of data fit between each other [20].

As demonstrated, for internal faults, stray capacitances combined to the transformer inductive effect result in TW amplitude variations and in oscillatory behaviors of DS filter outputs at Bus L, i.e., outputs are no longer well-behaved triangular/parabola-shaped signals. Such a feature can pose difficulties on TW-based applications, especially if TW amplitudes and polarities are required to be analyzed. Such oscillations are less prominent at Bus R, because the lines connected to such terminal result in $\Gamma_I \approx 1$, which favors TWI measurements. Hence, the first incident TW and the first fault-reflected TWs result in well-behaved triangular/parabola-shaped DS filter outputs, facilitating the analysis of TWIs. However, after some time, distorted TWs reflected from Bus L arrive, adding distortions to remote TW measurements as well. Finally, in the external fault cases at point F2, oscillating TW measurements with significant attenuation take place at both buses L and R. Since fault-launched TWs propagate through the transformer stray capacitances toward the line, TWs are distorted and attenuated, even for high C_{busbar}, resulting in oscillatory DS filter outputs.

V. Evaluation of TW-Based Applications

The classical double-ended TW-based fault location (DETWFL) method, as well as directional (TW32), overcurrent (TW50) and differential (TW87) protection elements are assessed in this section. As mentioned earlier, a validated TW filtering process is considered [21], allowing to calculate protection operating signals in a realistic way. Hence, the main steps of each function were externally implemented in a mathematical platform, taking PSCAD simulation records as input signals. By doing so, internal protection operating quantities could be assessed for each simulation, which would not be possible by using real devices whose outputs are typically limited to the tripping commands. Even so, although the authors did not have access to real TW devices, they recognize that using off-the-shelf TW solutions would be interesting as well, so that it is taken as a promising study for future works. Finally, it is important to mention that details on the evaluated TW-based protections can be found in [15]–[17], being only the main concepts of each function described here. In this evaluation stage, AG faults at F1, F2 and F3 with $\theta = 90^\circ$ are considered, varying R_f, d and stray capacitances, as explained earlier.

A. Double-Ended TW-Based Fault Location (DETWFL)

The classical DETWFL technique obtains the estimated fault distance $\tilde{d}$ by applying the formula [15]:

$$\tilde{d} = 0.5 \cdot [\ell - (t_R - t_L) \cdot v_p] \ , \tag{3}$$

being v_p the TW1/TW2 propagation velocity, and t_L and t_R the arrival instants of the first incident TWs at buses L and R, respectively. Here, v_p is calculated from the monitored line electrical parameters, resulting in $v_p = 295477.554$ km/s.

Since in fault location procedures $\tilde{d}$ is calculated for internal faults only, faults at point F1 with $d = 30$ km and 70 km are studied. In each case, busbar and transformer stray capacitances are varied, being the absolute error $|d - \tilde{d}|$ calculated. The obtained results are shown in Fig. 7.

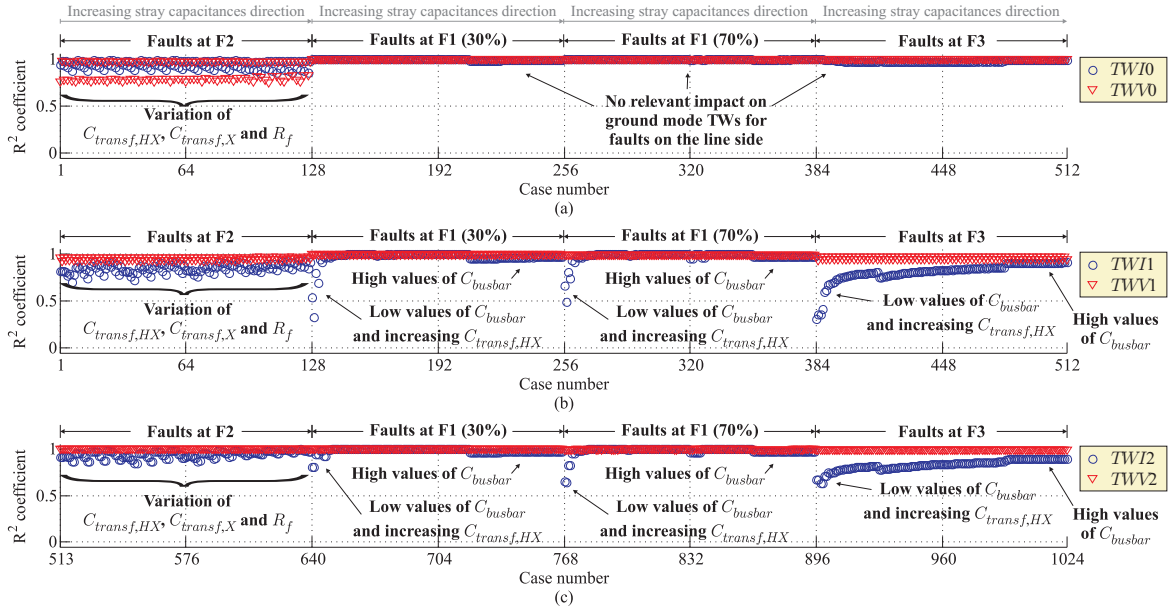

Fig. 5. Analyzing R^2 coefficients to evaluate similarity of modal filtered TWs for internal AG faults at points F1 (cases from 129 to 384), F2 (cases from 1 to 128) and F3 (cases from 385 to 512) and AB faults at points F1 (cases from 641 to 896), F2 (cases from 513 to 640) and F3 (cases from 896 to 1024): (a) TWI0s and TWV0s for an AG fault; (b) TWI1s and TWV1s for an AG fault; (b) TWI2s and TWV2s for an AB fault.

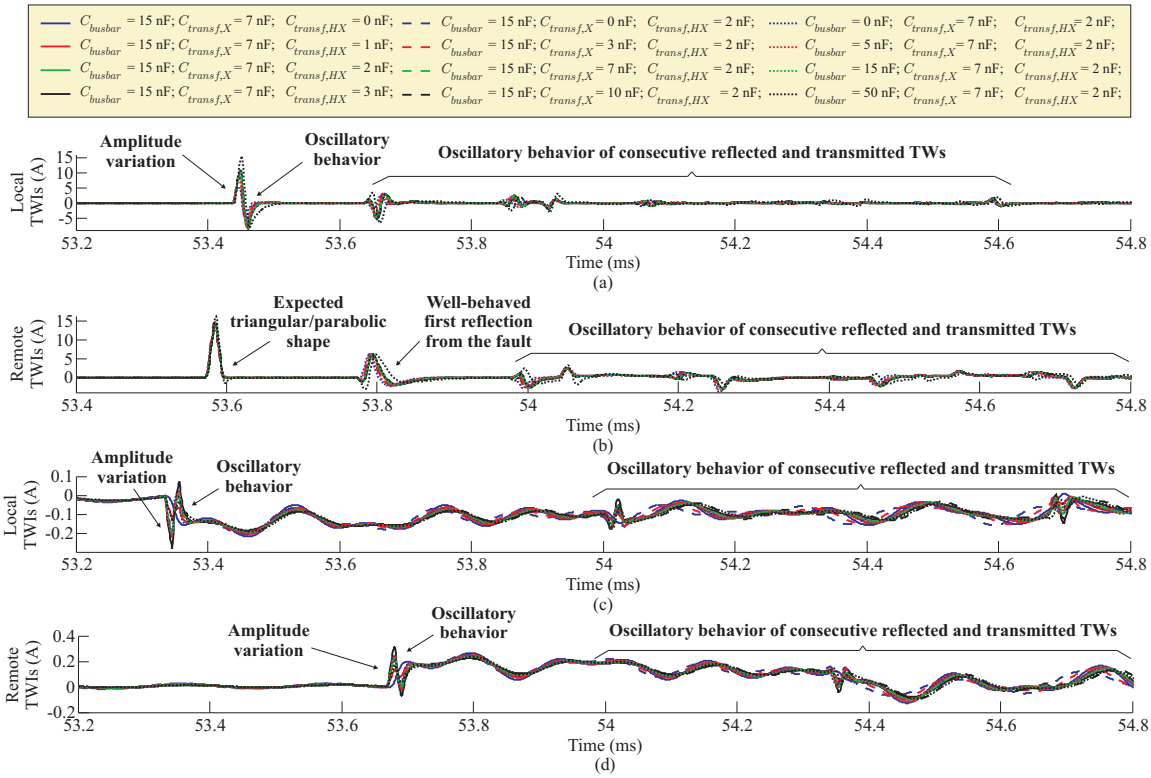

Fig. 6. Filtered TWs for different stray capacitances: (a) Local and (b) Remote TWIs for faults at F1; (c) Local and (d) Remote TWIs for faults at F2.

One can see that most errors shown in Fig. 7 are smaller than 600 m (two typical tower spans), except in few initial cases, which regard to low stray capacitances. In the evaluated cases, R_f was not critical, although it may be a problem depending on the TW detection methodologies used to support (3). Hence, it is concluded that the classical DETWFL method is effective in IBR-interconnecting lines, but if low stray capacitances take place, distortions and critical attenuation in measured TWs can affect TW detectors, adding errors especially in t_L and, consequently, in $\tilde{d}$.

B. TW-Based Directional Protection Function (TW32)

The TW32 element analyzed in this paper is reported in [17]. It consists of an improved version of classical TW32

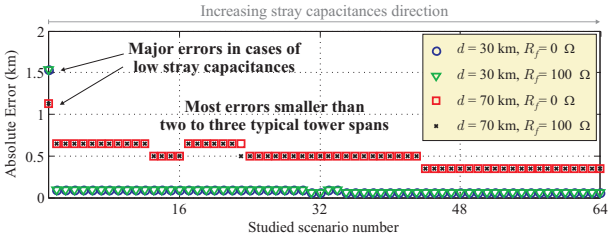

Fig. 7. DETWFL method performance in IBR-interconnecting lines.

function presented in [16], since it overcomes the need for analyzing voltage transients, which is a limiting factor due to the poor frequency response of capacitive voltage transformers [15]. Fig. 8 presents the main principles of such a function. In summary, when a fault takes place on the positive and negative voltage semi-cycles, negative and positive TWIs are launched on the line, respectively, but due to the current transformer polarity, they are measured as positive and negative TWs. Hence, a reliable torque can be calculated as the product between measured TWI and the voltage instantaneous value few samples before the TWI detection. By doing so, positive and negative torques are obtained for forward (FWD) and reverse (REV) faults, respectively.

The results obtained during the evaluation of the TW32 function are presented in Fig. 9 in terms of local and remote torques. As expected, the analyzed TW32 elements properly indicate FWD faults at Bus L for short-circuits applied at F1 and F3, and REV faults for short-circuits at point F2. On the other hand, at Bus R, the TW32 element correctly indicates FWD short-circuits for faults at points F1 and F2, whereas REV faults are detected for short-circuits at point F3. An important aspect regards the behavior of calculated torques. At Bus R, stable torques are obtained in all studied scenarios. However, at Bus L, calculated torques approximate to zero in the first cases of low stray capacitances. It results from the attenuation of TWIs, especially when low C_{busbar} values are considered. Even so, the overall behavior of the TW32 function indicates that such a protection element is promising for IBR-interconnecting lines, although cautious studies are recommended to define minimum pickup settings for torques, since they can present low values in the case of low C_{busbar}.

C. TW-Based Overcurrent Protection Function (TW50)

The TW50 function analyzes the amplitude of TWs at a given line terminal. It distinguishes faults on the low voltage transformer side from faults on the high voltage line side by evaluating the amplitude of TWIs. To do so, a TW50 pickup setting ($TW50P$) is proposed in [8], which is given by:

$$TW50P = 2 \cdot \sqrt{\frac{2}{3}} \cdot \delta \cdot \frac{V_{nom,L}}{Z_{s,min,X}} \cdot k \ , \qquad (4)$$

where δ is a passing TW coefficient, which represents the fraction of the wavefront that passes through the transformer stray capacitances to the high voltage line side (according to [8], $\delta = 0.05$ and 0.1 can be used), $V_{nom,L}$ is the rated system line-to-line voltage (here 500 kV), $Z_{s,min,X}$ is the smallest surge impedance found in the lines connected at the low

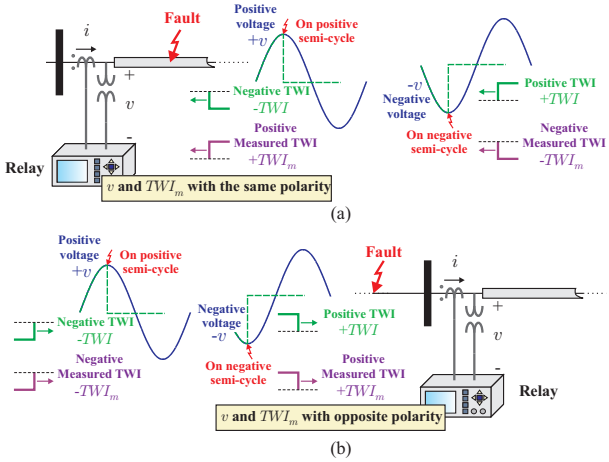

Fig. 8. Principles of the analyzed TW32 function: (a) FWD; (b) REV faults.

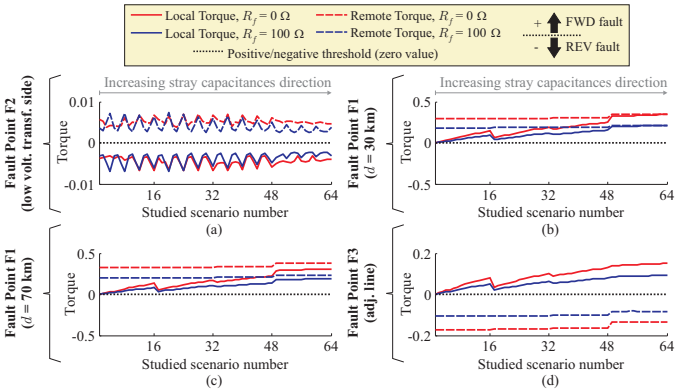

Fig. 9. Obtained results for the analyzed TW32 function considering faults at points: (a) F2; (b) F1 ($d = 30$ km); (c) F1 ($d = 70$ km); (d) F3.

voltage transformer side (according to [8], $Z_{s,min,X} \approx 350\ \Omega$ or $\approx 70\ \Omega$ can be used for overhead and underground lines, respectively), and k is a security margin (according to [8], $k = 1.5$ or 2 are appropriate).

Here, $TW50P$ is calculated using both δ values suggested in [8], adopting a conservative k margin equal to 2. It results in $TW50P = 2.916$ A_{sec} and 5.832 A_{sec}, which are used to assess the TW50 performance under the studied scenarios. Moreover, although the TW50 was originally proposed to be used only at the line terminal on the grid side [8], in this paper, the analysis is extrapolated to both monitored line terminals, allowing to assess the TW50 dependability also at Bus L. For the sake of simplicity, the amplitudes of aerial mode TWIs measured at buses L and R are called IL and IR, respectively.

The obtained results are presented in Fig. 10. From Figs. 10(a) and (b), it can be seen that the TW50 function was not sensitized neither at Bus L nor at Bus R for faults on the low voltage transformer side at point F2, irrespective of the used $TW50P$ value. On the other hand, for faults at point F1, according to Figs. 10(c), (d), (e), (f), (g) and (h), while all faults are properly detected at Bus R (grid side), there are cases in which the TW50 function do not operate at Bus L due to low stray capacitances and strong transformer inductive effect. In these scenarios, TWIs are very attenuated, even

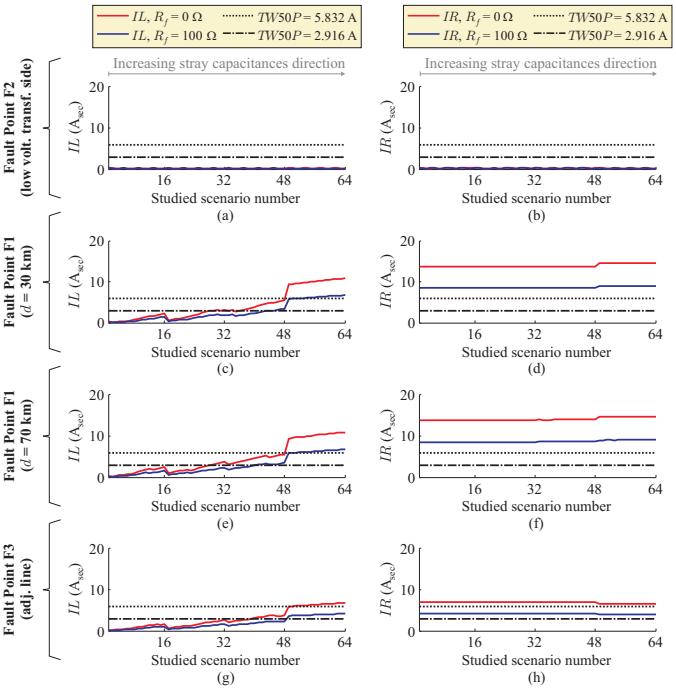

Fig. 10. Obtained results for TW50 function: IL for faults at (a) F2; (c) F1 ($d = 30$ km); (e) F1 ($d = 70$ km); and (g) F3; as well as IR for faults at (b) F2; (d) F1 ($d = 30$ km); (f) F1 ($d = 70$ km); and (h) F3.

being generated on the line side. Hence, IL values smaller than the pickup $TW50P$ are obtained, desensitizing the TW50 protection element at Bus L.

From the overall behavior of the TW50 element, it is concluded that such a function showed to be very promising for IBR-interconnecting lines, especially when applied at the remote bus at the grid side. Nevertheless, as the developers of such function recognize, the TW50 application at the IBR terminal deserves especial attention, since reliability issues may occur in cases of low busbar and transformer stray capacitances, depending on the chosen $TW50P$ setting. Even so, the authors emphasize that, if high busbar stray capacitances are expected at Bus L, the TW50 function can present a good performance, being quite useful to avoid blind zones close to the IBR terminal, when only non-unit protections are available [3].

D. TW-Based Differential Protection Function (TW87)

Fig. 11 shows internal and external fault cases to explain the main principles of TW87. As proposed in [16], differential $IDIF$ and restraining $IRST$ quantities are calculated from TWIs measured at buses L and R ($TWIL$ and $TWIR$, respectively). Basically, once the first incident TWI is detected in a given bus, an exit TWI is sought at the opposite line terminal after the line travel time τ. Hence, considering Fig. 11 as reference, $IDIF$ and $IRST$ can be calculated using:

$$IDIF = |TWIL(t) + TWIR(t - P)| \ , \tag{5}$$

$$IRST = \max(IRST1, IRST2) \ , \tag{6}$$

being $IRST1 = |TWIR(t) - TWIL(t - \tau)|$ and $IRST2 = |TWIR(t - \tau) - TWIL(t)|$ [16].

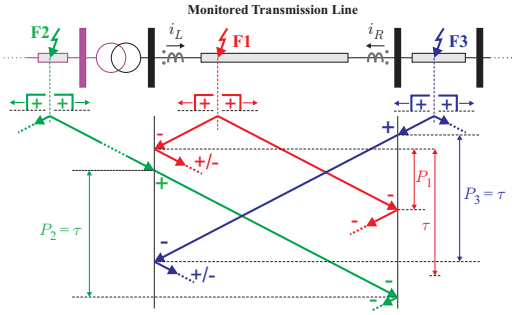

Fig. 11. Principles of the analyzed TW87 function.

Considering the polarities of current transformers, as shown in Fig. 11, for internal faults at F1, the first TWIs arriving at buses L and R have the same polarity, being spaced by a time period $P_1 < \tau$. Although positive and negative reflection coefficients Γ_I can be verified, depending on the busbar and transformer stray capacitances, in the worst case, measured TWs at Bus L are critically attenuated, but they do not invert their polarity. Thus, $IDIF$ tends to increase and $IRST$ to decrease for faults at F1. On the other hand, for the external faults F2 and F3, as the first incident TWIs at buses L and R have opposite polarities, being spaced by a time period $P_2 = P_3 = \tau$ (see Fig. 11), $IDIF$ decreases and $IRST$ increases, allowing to distinguish internal from external faults.

To issue a tripping command, the TW87 analyzes the following main conditions: C1) $IDIF > SLP \cdot IRST$; C2) $IDIF > I_{pk}$; C3) $\Delta d < m87 < \ell - \Delta d$; C4) $IL > I_{pk}$; and C5) $IR > I_{pk}$, where: SLP and I_{pk} are the slope and pickup settings, adjusted here to be 0.7 and 5.832 A_{sec} (according to the highest $TW50P$ value used during the analysis of the TW50 function), respectively; $m87$ is the per unit fault location, which is calculated in this paper from the previously analyzed DETWFL method as $m87 = \frac{d}{\ell}$; Δd is a security fault location zone around the monitored line terminals, set here as 0.03 pu to avoid confusion between close-in and far-end faults with external short-circuits; IL is the TWIL amplitude and IR is the TWIR amplitude, which have been already analyzed in the context of the TW50 function. The obtained results for the TW87 element are depicted in Fig. 12, but, since IL and IR have been already assessed in Section V-C, only the conditions C1, C2 and C3 are illustrated.

According to Figs. 12(a) and (b), the TW87 correctly restrains for external faults at point F2, since conditions C1, C2 and C3 are not satisfied. For internal fault cases at point F1, the results depicted in Figs. 12(c), (d), (e) and (f) reveal that, for solid faults, operating conditions C1, C2 and C3 are satisfied, resulting in the TW87 operation. However, it is also observed that, for $R_f = 100$ Ω, depending on the stray capacitance values, conditions C1 and C2 may lose sensitivity, depending on the chosen SLP and I_{pk} settings. Such a behavior is expected for TW functions, whose tripping commands are released only if high energy TWs are detected. It justifies the use of conditions C4 and C5, which would also restrain the TW87 operation for low busbar stray capacitance values (see Fig. 10). Even so, this is a point of attention, which must

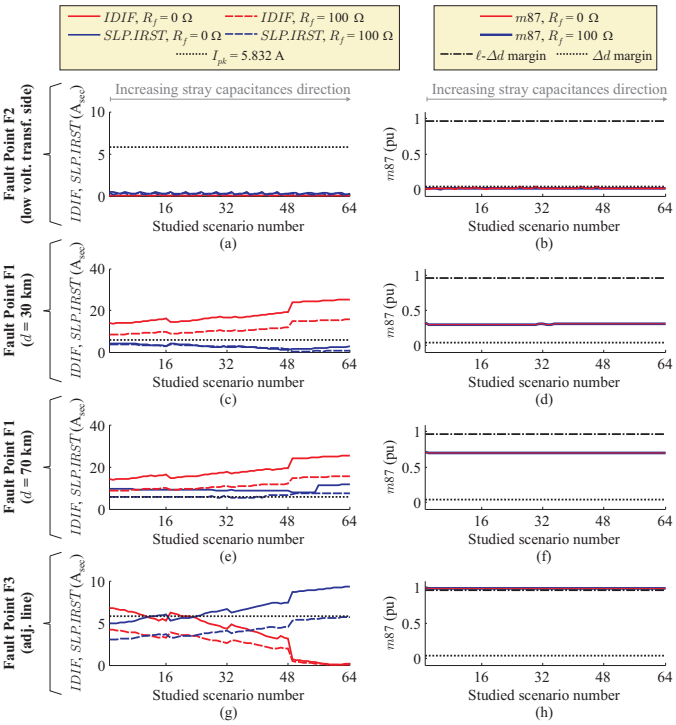

Fig. 12. Obtained results for TW87 function: $IDIF$ and $SLP \cdot IRST$ for faults at (a) F2; (c) F1 ($d = 30$ km); (e) F1 ($d = 70$ km); (g) F3; and $m87$ for faults at (b) F2; (d) F1 ($d = 30$ km); (f) F1 ($d = 70$ km); (h) F3.

be considered during the definition of SLP and I_{pk} settings. Finally, considering external faults at point F3, as shown in Figs. 12(g) and (h), the TW87 correctly restrains in most cases, but for low busbar stray capacitances, conditions C1 and C2 may incorrectly be satisfied. Nevertheless, conditions C3, C4 and C5 would properly restrain the TW87 operation, guaranteeing a secure protection decision.

The obtained results show that the TW87 is promising for IBR-interconnecting lines, but reliability and security issues may take place depending on values of the transformer and busbar stray capacitances. Thus, although correct operations of the TW87 function were observed in all cases, the authors recognize that transformer and busbar stray capacitances have an important influence on its performance, such that analyzing them before defining the TW87 settings is recommended.

VI. Conclusions

An assessment of DETWFL, TW32, TW50 and TW87 functions when applied to IBR-interconnecting lines is presented in this paper. A total of 1024 fault scenarios are studied via PSCAD simulations. Initially, similarity between TWs measured in systems with different IBRs with different control schemes is presented, and then, the effects of line terminal transformer and stray capacitances are investigated.

The obtained results reveal that TW-based protection and fault location functions are promising for applications in IBR-interconnecting lines. However, it is demonstrated that the line terminal power transformer and system stray capacitances are decisive for the performance of TW functions, since they can critically distort and/or attenuate TWs measured at the line terminal on the IBR side. In this sense, the analysis of transformer and busbar stray capacitances before defining settings of TW functions is strongly recommended (either for protection or fault location algorithms) to guarantee satisfactory sensitivity and to avoid security issues.

References

[1] A. Hooshyar, M. A. Azzouz, and E. F. El-Saadany, "Distance protection of lines connected to induction generator-based wind farms during balanced faults," *IEEE Transactions on Sustainable Energy*, vol. 5, no. 4, pp. 1193–1203, 2014.

[2] B. Kasztenny, "Line distance protection near unconventional energy sources," in *16th International Conference on Developments in Power System Protection (DPSP 2022)*, vol. 2022, 2022, pp. 224–229.

[3] F. Lopes, M. Davi, K. Silva, R. Filho, A. Neto, R. Reis, T. Honorato, P. Junior, M. Oleskovicz, and F. Vasquéz, "From hertz to megahertz: Lessons learned about the impact of inverter-based wind turbine generators on the protection of interconnecting lines," *CIGRE Paris Session*, 2022.

[4] ENTSO, *ENTSO-E network code for requirements for grid connection applicable to all generators*, Belgium, 2013.

[5] USA Federal Energy Regulatory Commission, *Interconnection for wind energy Docket No. RM05-4-001, Order No. 661-A*, USA, 2005.

[6] M. LeBlanc, L. Evans, P. Gardner, and N. Scott, "Canadian grid code for wind development: review and recommendations," 2006.

[7] F. Lopes, J. Costa, T. Honorato, R. Toledo, L. Gama, P. Pereira, G. Salge, and M. Davi, "Busbar capacitance modeling effects during relay testing procedures for transmission lines interconnecting wind power plants," *Journal of Control, Automation and Electrical Systems*, vol. 33, no. 2, pp. 541–549, 2022.

[8] B. Kasztenny, M. Mynam, S. Marx, and R. Barone, "Traveling-wave overcurrent-a new way to protect lines terminated on transformers," in *75th Annual Georgia Tech Protective Relaying Conf.*, 2022, pp. 1–13.

[9] N. Miller, J. Sanchez-Gasca, W. Price, and R. Delmerico, "Dynamic modeling of ge 1.5 and 3.6 mw wind turbine-generators for stability simulations," in *2003 IEEE Power Engineering Society General Meeting (IEEE Cat. No.03CH37491)*, vol. 3, 2003, pp. 1977–1983 Vol. 3.

[10] T. Kauffmann, U. Karaagac, I. Kocar, S. Jensen, E. Farantatos, A. Haddadi, and J. Mahseredjian, "Short-circuit model for type-iv wind turbine generators with decoupled sequence control," *IEEE Transactions on Power Delivery*, vol. 34, no. 5, pp. 1998–2007, 2019.

[11] "Ieee standard for interconnection and interoperability of inverter-based resources (ibrs) interconnecting with associated transmission electric power systems," *IEEE Std 2800-2022*, pp. 1–180, 2022.

[12] F. M. Magalhães Júnior and F. V. Lopes, "Mathematical study on traveling waves phenomena on three phase transmission lines – part i: Fault-launched waves," *IEEE Trans. on Power Delivery*, vol. 37, no. 2, pp. 1151–1160, 2022.

[13] ——, "Mathematical study on traveling waves phenomena on three phase transmission lines – part ii: Reflection and refraction matrices," *IEEE Trans. on Power Delivery*, vol. 37, no. 2, pp. 1161–1170, 2022.

[14] A. Greenwood, *Electrical transients in power systems*. New York, NY (USA); John Wiley and Sons Inc., 1991.

[15] M. M. Saha, J. Izykowski, and E. Rosolowski, *Fault location on power networks*. Springer, 2010, vol. 2.

[16] E. Schweitzer, B. Kasztenny, and M. Mynam, "Performance of time-domain line protection elements on real-world faults," in *69th IEEE Annual Conference for Protective Relay Engineers*, 2016, pp. 1–17.

[17] K. Nayak, S. Jena, and A. K. Pradhan, "Travelling wave based directional relaying without using voltage transients," *IEEE Transactions on Power Delivery*, vol. 36, no. 5, pp. 3274–3277, 2021.

[18] E. Schweitzer, A. Guzmán, M. Mynam, V. Skendzic, B. Kasztenny, and S. Marx, "Locating faults by the traveling waves they launch," in *67th IEEE Annual Conf. for Protective Relay Engineers*, 2014, pp. 95–110.

[19] F. Lopes, E. Leite, J. P. Ribeiro, L. Lopes, and A. Piardi, "Using the differentiator-smoother filter to analyze traveling waves on transmission lines: Fundamentals settings and implementation," in *Intern. Conf. on Power Systems Transientes*, 2019, pp. 1–6.

[20] M. Spiegel, J. Schiller, and A. Srinivasan, *Probability and statistics*. McGraw-Hill, Schaum's-Outlines, 2020.

[21] E. P. A. Ribeiro, F. V. Lopes, J. P. G. Ribeiro, and E. J. S. Leite, "Atp/models differentiator-smoother filter model validated using actual time-domain relay," in *2018 Workshop on Communication Networks and Power Systems (WCNPS)*, 2018, pp. 1–4.